Research Article Vol. 31, No. 16 / 31 Jul 2023 / Optics Express 26463
Optics EXPRESS

Simultaneous enhancement of the bandwidth and responsivity in high-speed avalanche photodiodes with an optimized flip-chip bonding package

NASEEM,[1] NAN-WEI CHEN,[2] SYED HASAN PARVEZ,[1] ZOHAUDDIN AHMAD,[1] SEAN YANG,[3] H-S CHEN,[3] HSIANG-SZU CHANG,[3] JACK JIA-SHENG HUANG,[3] AND JIN-WEI SHI[1,*]

[1]*Department of Electrical Engineering, National Central University, Jhongli, 320, Taiwan*
[2]*Department of Electrical Engineering, Yuan Ze University, Jhongli, 320, Taiwan*
[3]*Source Photonics, No. 46, Park Avenue 2nd Rd., Science-Based Industrial Park, Hsinchu, Taiwan*
[*]*jwshi@ee.ncu.edu.tw*

Abstract: The enhancement in responsivity of photodiodes (PDs) or avalanche photodiodes (APDs) with the traditional flip-chip bonding package usually comes at the expense of degradation in the optical-to-electrical (O-E) bandwidth due to the increase of parasitic capacitance. In this work, we demonstrate backside-illuminated $In_{0.52}Al_{0.48}As$ based APDs with novel flip-chip bonding packaging designed to relax this fundamental trade-off. The inductance induced peak in the measured O-E frequency response of these well-designed and well-packaged APDs, which can be observed around its 3-dB bandwidth (~30 GHz), effectively widens the bandwidth and becomes more pronounced when the active diameter of the APD is aggressively downscaled to as small as 3 µm. With a typical active window diameter of 14 µm, large enough for alignment tolerance and low optical coupling loss, the packaged APD exhibits a moderate damping O-E frequency response with a bandwidth (36 vs. 31 GHz) and responsivity (3.4 vs. 2.3 A/W) superior to those of top-illuminated reference sample under 0.9 V_{br} operation, to attain a high millimeter wave output power (0 dBm at 40 GHz) and output current (12.5 mA at +8.8 dBm optical power). The excellent static and dynamic performance of this design open up new possibilities to further improve the sensitivity at the receiver-end of the next-generation of passive optical network (PON) and coherent communication systems.

1. Introduction

Given the ever-increasing demand for high bandwidth in modern communication networks, especially in the 5 G and cloud networks, the development of passive optical network (PON) technology has become crucial. An IEEE task force is currently standardizing the 50 G PON specifications required to meet the demands of continuously increasing data traffic [1,2]. In addition to the issue of chromatic dispersion encountered at 50 Gbit/s, which can be significantly mitigated by operating around the 1.31 µm optical window with a negligible dispersion-free wavelength spectrum, two other major issues remain to raising PON rates from 10 to 50 Gbit/sec. The first is to maintain the link budget and the second is to identify components that have sufficient bandwidth and linearity and are mature enough to be used in PON systems. One possible way to improve the link budget and cost-effectiveness in 50G-PONs is to use low-cost directly modulated lasers (DML) and avalanche photodiodes (APD) [1]. In the receiver-side of 50 G PONs, it is highly desirable to use high-speed and wide dynamic range APDs [2] embedded in a burst-mode receiver because of the large tolerance in the received optical power level [3]. Moreover, as compared to using p-i-n PD counterparts in the receiver, the APD can provide better sensitivity

#494510 https://doi.org/10.1364/OE.494510
Journal © 2023 Received 1 May 2023; revised 12 Jun 2023; accepted 17 Jul 2023; published 25 Jul 2023

Optics EXPRESS

performance leading to a larger link budget. In addition to the intensity modulation and direct detection (IMDD) scheme, coherent communication schemes have become an alternative solution for >100 Gbit/sec data communication [3,4]. In a coherent receiver-end, APDs can provide better sensitivity performance with a lower optical LO pumping power than those of the traditional p-i-n PDs [5,6]. However, in order to meet the needs for such high-speed operation (> 50 Gbuad), both the absorption and multiplication layer thicknesses in the traditional $In_{0.52}Al_{0.48}As$ based APDs must be aggressively downscaled, which limits the responsivity performance for wide bandwidth performance (>30 GHz) [7,8] and is accompanied by a pronounced leakage current (~1 μA) [8]. In order to improve the responsivity performance in high-speed APDs, a backside-illuminated structure with a flip-chip bonding package is usually preferred [9]. With such a scheme, the topmost metal contact of the APD can serve as a reflector enhancing the photo-absorption process. However, in comparison to the top-illuminated reference device, the flip-chip bonding packaged device usually has a higher responsivity but less bandwidth due to the additional parasitic capacitance after packaging. Some alternative solutions, such as the addition of refracting facets [10] or the installation of a 45° mirror beneath the APD chip [7], have been demonstrated to fold the optical absorption path and minimize the package induced parasitic capacitance. However, the integration of a flip-chip bonding package with a well fabricated substrate lens is still a very attractive alternative because it offers the largest alignment tolerance and minimum size after package among all the reported PD/APD packaging technologies [9]. In this work, we demonstrate a $In_{0.52}Al_{0.48}As$ based backside-illuminated APD with a novel flip-chip bonding package which is designed to relax the fundamental trade-off between responsivity and bandwidth. After optimizing the layout on the *Aluminum Nitride* (AlN) carrier for flip-chip bonding, significant peaking in the measured optical-to-electrical (O-E) frequency response is observed for an APD with a very small active diameter (3 μm), which arises due to the additional inductive effect of our well-designed planar circuit. With a reasonable active window diameter of 14 μm for low optical coupling loss, the packaged device exhibits a more moderate damping O-E frequency response and superior bandwidth (36 vs. 31 GHz) and responsivity (3.4 vs. 2.3 A/W) to those of the top-illuminated reference device under 0.9 V_{br} operation. In terms of high-power performance, with this device package, we are also able to attain a record-high millimeter wave output power (0 dBm) at 40 GHz with a high saturation current (12.5 mA at +8.8 dBm optical power) among all those reported for high-speed APDs. Compared with our previous work [11], this study gives a more detailed discussion of our flip-chip bonding package and further improvements in the bandwidth and MMW output power. The excellent performance in terms of speed and saturation current of this device ensure its applicability for advanced high-speed receivers in PON or coherent system.

2. Design and fabrication of the device structure

A conceptual cross-sectional view of the device structure is shown in Fig. 1(a); please note that for clarity, the device is not drawn to scale. The exact doping density values and the thickness of each layer are also specified here. The topmost layer is a p + -$In_{0.53}Ga_{0.47}As$ contact layer, followed by a p + -InP window layer, a p-type partially depleted $In_{0.53}Ga_{0.47}As$ absorber, composite p-type $In_{0.52}Al_{0.48}As$/InP charge layers, a dual intrinsic $In_{0.52}Al_{0.48}As$ multiplication (M-) layer, an n-type $In_{0.52}Al_{0.48}As$ charge layer, a thick InP collector (transport) layer, and the bottommost InP n + contact layer. The layers are grown on a semi-insulating (S.I.) InP substrate. To satisfy the demands for APD bandwidth, the thicknesses of the absorber and total M-layer are further decreased, as explained in our previous work [5]. Typically, in the traditional APD structure, this increase in bandwidth would come with a degradation in the responsivity and cause a rise in the dark current [7,8]. To alleviate the trade-off between speed, dark current and responsivity, we implemented a dual M-layer structure [5,12,13]. This structure divides the M-layer into two segments, labeled as the 1st and 2nd M-layer in Fig. 1(a), with an added charge control layer

Optics EXPRESS

between them. This design results in a stepped electric field profile, with the majority of the avalanche process confined to the extremely thin 2nd M-layer, which has the highest E-field across the entire epi-structure. This leads to a short avalanche delay time, high GBP, and low excess noise. Compared to the traditional APD's direct scaling down of a single M-layer to the same thickness as our 2nd M-layer, the inclusion of the 1st M-layer in our design can effectively suppress the tunneling leakage process resulting in lower overall dark current.

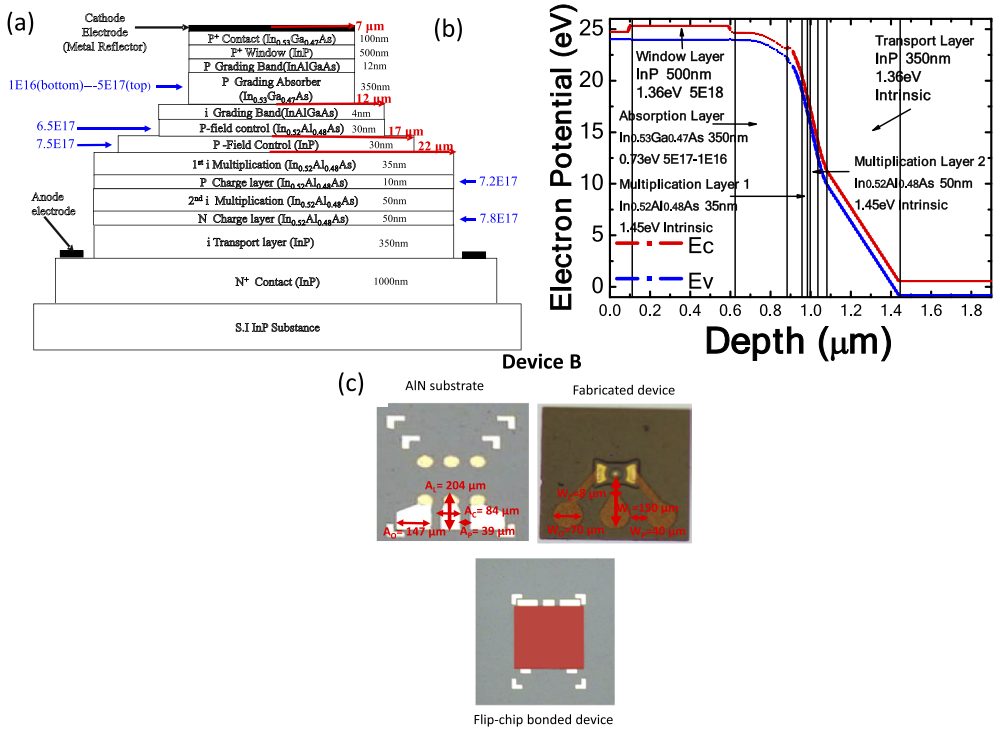

Fig. 1. (a). Conceptual cross-sectional view of the fabricated device; (b) simulated band diagram of the demonstrated dual M-layer APD; (c) top-views of fabricated device B before and after flip-chip bonding packaging. The doping density unit in (a) is cm^{-3}

To prevent edge breakdown, a composite charge layer design ($In_{0.52}Al_{0.48}As$/InP) is utilized to ensure that the electric field at the bottom (2nd) M-layer's side wall reaches zero [14]. To alleviate the RC-limited bandwidth constraint and increase the APD's active diameter for better alignment tolerance in the APD package, an InP collector layer is incorporated beneath the M-layer. The use of an InP layer rather than an $In_{0.52}Al_{0.48}As$ based collector layer enables a larger overshoot electron drift-velocity [15], resulting in a relaxation of the trade-off between the device active area and the RC-limited bandwidth.

Furthermore, the p-side up structure of our design can provide better output saturation power than the inverted p-side down APD structure [5], mainly because the bottom-most InP substrate is in close proximity to the second M-layer with the highest E-field, which provides more effective heat sinking for the device. Figure 1 (a) shows the quintuple mesa structure with the 14 μm first mesa used in our devices. For more detailed information about our epi-layer and device mesa structures, please refer to our previous work [5]. Figure 1 (b) shows the simulated band diagram of our demonstrated APD under 0.9 V_{br} operation. As can be seen, by properly adjusting the doping density in each charge layer, most of the electric (E)-field can be confined in the thin 1st and 2nd M-layers for a pronounced avalanche process, as discussed above. Moreover,

Optics EXPRESS

the E-field in the other layers is also well controlled at less than their critical fields, to avoid the occurrence of undesired breakdown processes in the absorption and collector layers. The flip-chip bonding package of the demonstrated APD is implemented on the AlN carrier substrate, which has excellent thermal and microwave characteristics. The layout of the metal pads on the carrier substrate usually plays an important role on the net optical-to-electrical (O-E) bandwidth of the packaged PD or APD module [16]. Altogether, the influence of different layouts on the speed performance for three kinds of device structures was investigated. All three devices shared the same epi-layer structure, as shown in Fig. 1 (a). Devices A and B had different flip-chip bonding package layouts while device C was the top-illuminated reference sample [5]. Figure 1(c) shows photos of the metal pads on the AlN carrier, and top-views of device B, before and after flip-chip bonding. Both devices A and B adopt the co-planar waveguide (CPW) structures in the design of the metal pads on the AlN carrier and InP substrates but the geometric sizes are different. The sizes and names of every part of the metal pad layout of device B are specified in Fig. 1 (c). In the layout of device A, we increased the lengths of the center metal stripes (A_L and W_L), narrowed their widths (A_c), and widened the widths of the air gaps (A_p and W_p) in order to increase the characteristic impedance and effective inductance (per unit length) of the CPW transmission lines [17]. This layout compensates for the RC-limited bandwidth of the active PD parts so that an improvement in the high-speed performance of device A can thus be expected, which will be discussed later.

3. Measurement results

Figures 2(a) through (c) show the bias-dependent dark current, photocurrent, and operation gain of devices A to C, respectively, which were measured at an optical wavelength of 1.31 μm under various optical pumping powers. The measured breakdown voltage (V_{br}) was observed to be approximately -26 V, for all three devices. The APDs demonstrated here show a much lower dark current (around 0.2 vs. > 1 μA at 0.9 V_{br}) compared to those reported for other APDs, with close values of 3-dB O-E bandwidth [7,8]. This improvement in the dark current can be attributed to the unique design of the cascaded M-layer and the addition of a special composite charge layer, as illustrated in Fig. 1, which eliminates edge breakdown [14]. At a low optical pumping power of 10 μW and an optical wavelength of 1.31 μm, the measured responsivity of device A to C is around 3.4, 3.1 and 2.3 A/W, respectively. The devices (A and B) with flip-chip bonding packages have a higher responsivity (3.4 vs. 2.3 A/W) due to the folding of the optical absorption path through the topmost metal contacts which function as reflectors. By assuming the responsivity measured at the punch-through voltage (V_{pt}) as the unit gain of each device, the corresponding gain of devices A, B, and C at 0.9 V_{br} is 6.93, 6.88, and 7.67, respectively. At the same optical pumping power (-20 dBm), we can clearly see that the maximum gain for device A is more than ten times larger (150 vs. 14 [18]) than that of its III-V [8] and Si-Ge [18] counterparts, as well as having a higher responsivity. This enhancement in performance can be attributed to the lower dark current and the more prominent avalanche process enabled by our dual M-layer design. The gain versus bias voltage of our device at various optical pumping power levels (ranging from 1 to 1000 μW) is also included in Fig. 2 for reference. As can be seen, there is a dramatic reduction in the operation gain when the optical pumping power increases from 1 to 50 μW due to the space-charge screening effect in the absorption layer [13]. Nevertheless, the operation gain remains nearly invariant at higher optical pumping power levels (> 100 μW). This is indicative of its good linearity performance for coherent receiver applications, which usually need to be operated under mW optical local oscillator (LO) pumping power levels [12].

Figures 3 and 4 show the bias-dependent O-E frequency responses of all three devices measured under low (10 μW) and high (1 mW) optical pumping powers, respectively, at the 1.55 μm wavelength. As can be seen, the measured 3-dB bandwidths for devices A, B and C are around 36, 27 and 30 GHz respectively. Device B experienced a degradation in O-E bandwidth

Optics EXPRESS

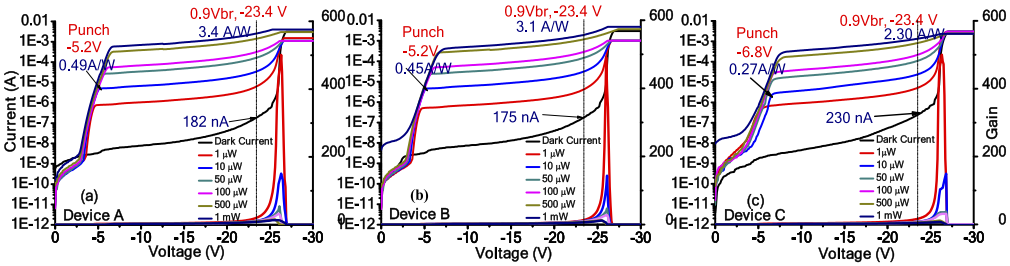

Fig. 2. Measured dark current, photocurrent, and operation gain versus bias voltage under different optical pumping powers at the 1.31 μm wavelength for all three APDs: (a) Device A, (b) Device B and (c) Device C.

(27 vs. 30 GHz) compared to reference device C under the same bias of 0.9 V_{br}, which can be attributed to the flip-chip bonding package-induced parasitic capacitance, as discussed earlier. On the other hand, device A, with the optimized flip-chip bonding layout, not only demonstrated the highest responsivity (3.4 vs. 3.1 and 2.3 A/W) but also exhibited the widest 3-dB bandwidth (36 vs. 27 and 30 GHz) among the three devices. Moreover, compared with the high-performance Si/Ge APD counterparts with the same 14 μm window size [18], which operate at around the same responsivity 3.5 (6.5) A/W, the 3-dB O-E bandwidth of our demonstrated device A is superior (36 (28) vs. 28 (22) GHz). On the other hand, under high (1 mW) optical power illumination, these three devices (A to C) can maintain invariant 3-dB O-E bandwidths of 36, 27 and 30 GHz at 0.9 V_{br}, respectively. Overall, the excellent static, as discussed in Fig. 2, and dynamic high-power performance indicate the good linearity and wide dynamic range of the demonstrated APDs for coherent receiver applications.

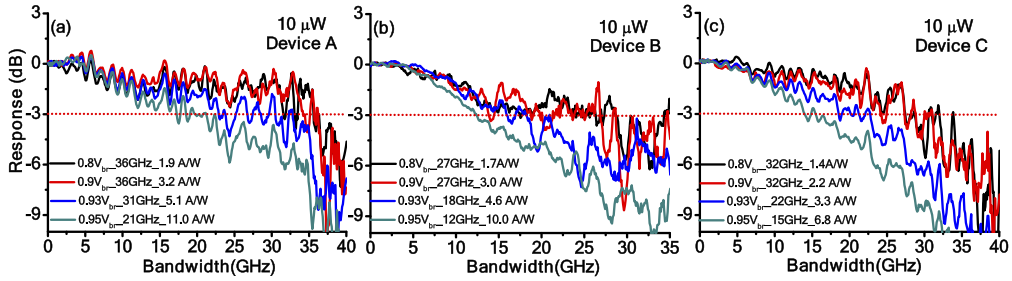

Fig. 3. Bias dependent O-E frequency responses of Devices (a) A (b) B, and (c) C measured under a low 10 μW optical pumping power at the 1.55 μm wavelength.

The superior O-E bandwidth performance of device A compared to device B is mainly due to the further optimization of the layout of both the metal pads integrated with the active PD and on the AlN carrier substrate, as illustrated in Fig. 1 (c). The inductive peaking effect arising from the layout of device A effectively compensates for the RC-limited bandwidth, which leads to an enhancement of the net O-E bandwidth. Similar concepts have been applied in the metal pad design of backside-illuminated high-speed and high-power PDs for bandwidth enhancement [19,20]. The measured frequency responses of the reflection coefficient of S parameters (S_{11}) for devices A and B with different active mesa diameters before flip-chip bonding are shown in Fig. 5. As can be seen, device A produces a longer trace on the Smith Chart than does device B, in the same frequency sweeping range (40 MHz to 40 GHz), due to the increase of its W_L.

Figures 6 (a) and (b) show the measured S_{11} parameters of these two devices (A and B) with different active diameters of 10 and 14 μm, respectively, after flip-chip bonding, respectively. We

Optics EXPRESS

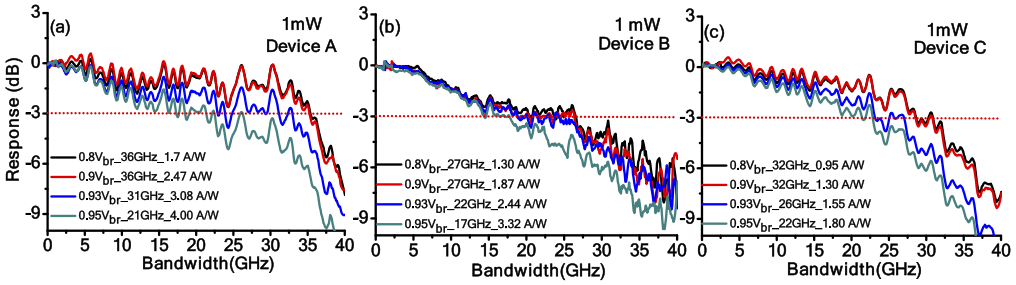

Fig. 4. Bias dependent O-E frequency responses of Devices (a) A (b) B, and (c) C measured under a high 1 mW optical pumping power at the 1.55 µm wavelength.

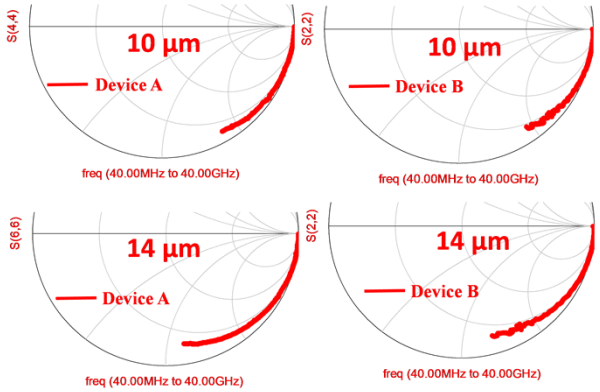

Fig. 5. The measured frequency response of the reflection coefficients of S parameters (S_{11}) for devices A and B which have different active mesa diameters, before flip-chip bonding.

can clearly see that regardless of the change in the size of the active mesa, device A exhibits longer trace lengths than does device B, as expected. Furthermore, the device A traces are closer to the outer boundary of Smith Chart, the implication being that the whole packaged APD module behaves more like an ideal capacitor with superior RF characteristics to those of device B. Figure 6 (c) shows the simulated S_{11} traces on the Smith chart of devices A and B with the same active mesa diameter of 14 µm. The trend of the simulation results clearly matches the measurement results. In the simulation, the passive metal pads on the InP and AlN carrier substrates are simulated as 3-D structure, for full-wave analysis with the HFSS tool [21]. On the other hand, the equivalent circuit model is applied to simulate the core part of the active APD, which can be directly extracted by the fitting process of the measured S_{11} parameters of the APD as shown in Fig. 5. The S parameters of the whole packaged module can be obtained by combining the S parameter matrix for the extracted equivalent circuit model with the 3-D full-wave analysis results [22,23].

Figures 7 (a) and (b) show the 3-D structure of device B used for the full-wave analysis and the extracted equivalent circuit model. The inserted Table shows the extracted values of circuit elements. In order to study the influence of the active mesa diameter on the bandwidth of the packaged module, samples of device A with 3 different diameters (3, 10, and 14 µm) were fabricated and tested. Figures 8 (a) to (c), respectively, show the bias-dependent dark current, photocurrent, and operation gain under various optical pumping powers for device A with 3 different active mesa diameters as specified. The optical wavelength was fixed at 1.31 µm. As can be seen, when the active mesa diameter is downscaled to 3 µm, there is a significant increase of the coupling loss and degradation of the responsivity.

Optics EXPRESS

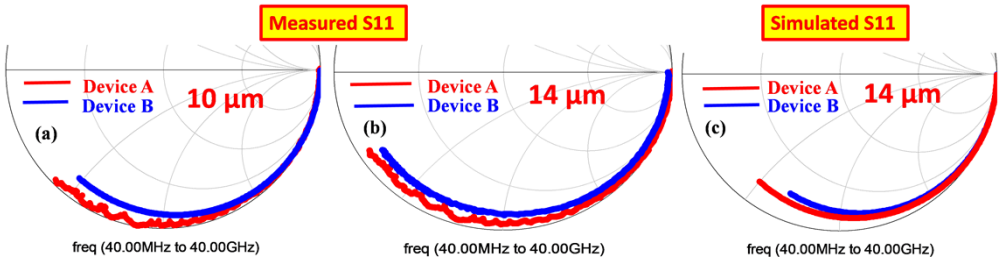

Fig. 6. The measured S_{11} parameters of Devices A and B with different active diameters of (a) 10 and (b) 14 μm after flip-chip bonding packaging, and (c) the simulated traces with an active diameter of 14 μm.

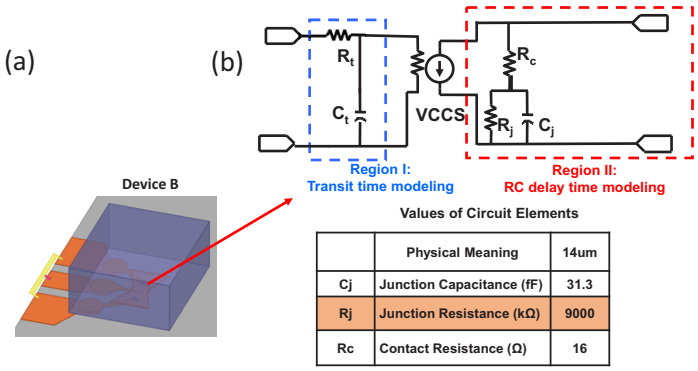

	Physical Meaning	14um
Cj	Junction Capacitance (fF)	31.3
Rj	Junction Resistance (kΩ)	9000
Rc	Contact Resistance (Ω)	16

Fig. 7. (a) The 3-D structure of device B used for full-wave analysis and (b) the extracted equivalent circuit model. The inserted table shows the extracted values of the circuit elements.

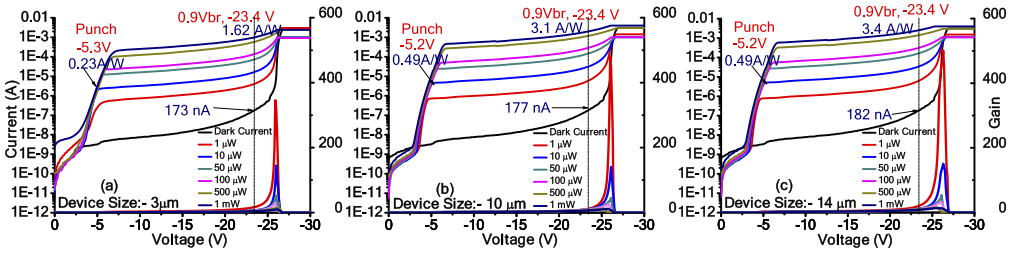

Fig. 8. The bias-dependent dark current, photocurrent, and operation gain obtained under various optical pumping powers at the 1.31 μm wavelength for devices A with active mesa diameters of: (a) 3, (b) 10, and (c) 14 μm.

Optics EXPRESS

Figures 9 (a) to (c) depict the measured bias-dependent O-E frequency responses of the three devices described above, under an optical pumping power of 1 mW at the 1.55 μm wavelength. As can be seen, the package induced resonance is most pronounced for device A with its miniaturized size (3 μm diameter), among these three devices. On the other hand, for the devices with larger active diameters (10 and 14 μm), the measured O-E frequency responses show moderate damping. Compared with the light damping trace for the 3 μm diameter APD, such moderate damping indicates that the extra noise induced by the peaking of the frequency response for bandwidth enhancement has been well balanced. Furthermore, this supports the idea that the flip-chip bonding structure of device A has been optimized for APDs with popular sizes of active diameter (> 10 μm), with consideration of low-loss coupling and easy optical alignment for the package.

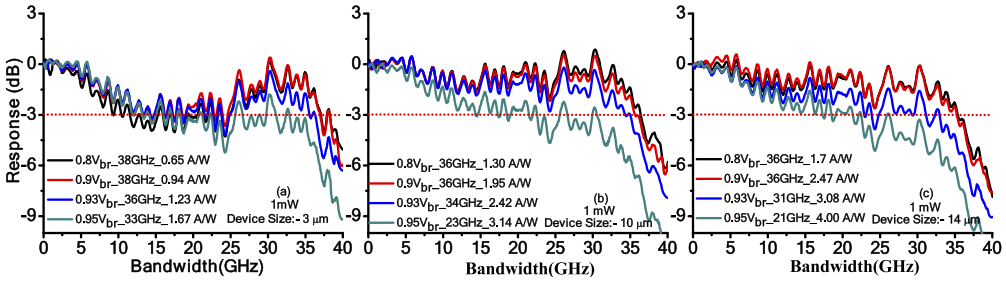

Fig. 9. Bias dependent O-E frequency responses measured under a high 1 mW optical pumping power at the 1.55 μm wavelength for Device A with different active mesa diameters of: (a) 3, (b) 10, and (c) 14 μm.

Figures 10 (a) to (c) show the photo-generated MMW output saturation power measured with the heterodyne beating setup at a beating frequency of 40 GHz for device A with 3 different active diameters, 3, 10, and 14 μm, respectively. All exhibit very close values of saturation current at 12 mA and a maximum output RF power of around 0 dBm under 0.9 V_{br}. This corresponds to a high launched optical power at +8.8 dBm for device A with a 10 μm active diameter. The MMW power achieved at 40 GHz should be the highest ever reported in high-speed APDs at telecommunication wavelengths [5,6,24–28]. Figure 11 (a) shows the measured 3-dB bandwidth versus multiplication gain (M_G) of device A with active diameters of 10 and 14 μm and device C. The values of the gain-bandwidth product (GBP) under $M_G = 10$ and the extremely high gain of these three devices are all specified. It can be clearly seen that, with our optimized flip-chip bonding layout, we can have improvements in the GBP under high-sensitivity operation ($M_G = 10$) as compared to those of top-illuminated reference sample (device C) and with an unprecedentedly large maximum GBP of up to 0.9 THz. Figure 11 (b) depicts the corresponding measured O-E frequency responses under low input power (10 μW) for Device A with 10 and 14 μm, and Device C with 14 μm active window diameters. Table 1 shows the benchmark reported for device A and for other high-speed APDs. Here, the values of the bandwidth and responsivity, which appear in parentheses, represent the measurement results obtained from the same APD but at a higher reverse bias voltage (> 0.9 V_{br}). In addition, in the bottom row, the test conditions specified for optical input and RF output saturation power performance, for each different device are specified in parentheses. The optical saturation represents the maximum input optical power value which leads to saturation of the output photocurrent. The optical overload stands for the damage threshold for maximum input optical power onto the APD. Thanks to the novel dual M-layer design with the optimized flip-chip bonding package, with device A, we can attain the lowest dark current, very-high bandwidth-responsivity product, and largest saturation optical power with the highest MMW output power at 40 GHz among those reported for APDs.

Optics EXPRESS

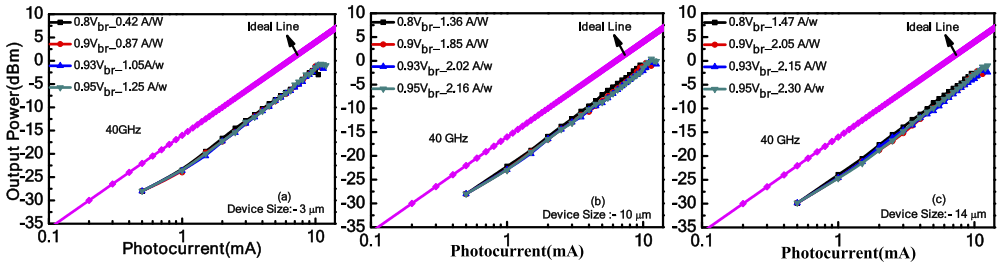

Fig. 10. Measured photo generated RF power versus photocurrent, at a frequency of 40 GHz for heterodyne beating under different V_{br} for Device A with different active mesa diameters of: (a) 3, (b) 10, and (c) 14 μm.

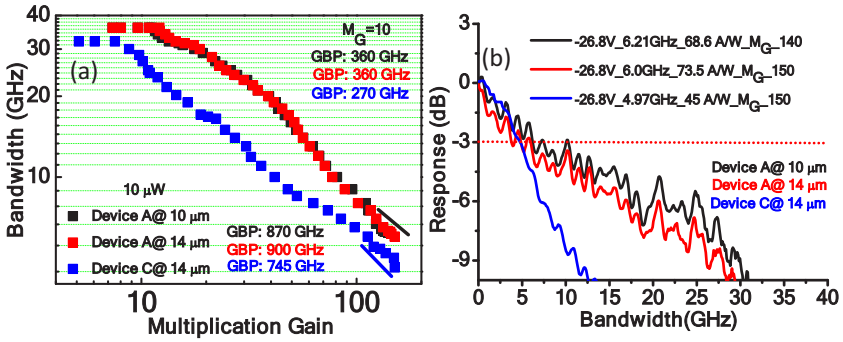

Fig. 11. (a) The measured 3-dB O-E bandwidths versus multiplication gain and (b) O-E bandwidth at low (10 μW) optical pumping powers and under extremely high gain for the Device A with 10, 14 μm and Device C with 14 μm active window diameters.

Table 1. Benchmark high performance APD performance

Parameter	NTT	SiFotonics Technology	SEDI, JAPAN	Intel Corporation	HHI, Berlin, Germany	HHI, Berlin, Germany	This work
Reference	7	18	26	27	28	6	
Type	Backside illuminated	Topside-illuminated (Reflector on Backside)	Waveguide	Waveguide	Waveguide	Waveguide	Backside-Illuminated
Window Size	14 μm	20 μm					14 μm
Dark Current (0.9 V_{br})	2 μA	0.9 μA	8 μA	1.4 μA	1 μA	400 nA	175 nA
Responsivity	1.95 A/W	3.53 (6.5) A/W	3.6 (9) A/W	3.42 A/W (Exclude coupling loss)	0.9 (1.52) A/W	1.3 (3.25)A/W	3.4 (6.52) A/W
Bandwidth	28 GHz	28 (22) GHz	38(24) GHz	45.8 GHz	37 (29) GHz	27 (24) GHz	36 (28) GHz
Optical Input or RF Output Saturation Power	-6.3 dBm (Optical Saturation)	< 0 dBm (Optical Overload)	-	-	-	-6 dBm at 20 GHz (RF Output)	+8.8 dBm (Optical Saturation) 0 dBm at 40 GHz (RF Output)

Optics EXPRESS

4. Conclusions

In conclusion, by combining our dual M-layer design with our advanced flip-chip bonding package, which is aimed at balancing the 3-dB bandwidth and heavy damping of O-E frequency responses for moderate sized (~14 μm) APDs with low optical coupling loss. The demonstrated device simultaneously exhibits a low dark current (175 nA), wide 3-dB bandwidth at 36 GHz, high responsivity 3.4 A/W, high saturation current of 12 mA, and high MMW output power (0 dBm at 40 GHz) under operation at 0.9 V_{br}.

Funding. National Science and Technology Council (110-2622-E-008-016-).

Disclosures. The authors declare no conflicts of interest.

Data availability. Data underlying the results presented in this paper are not publicly available at this time but may be obtained from the authors upon reasonable request.

References

1. M. Tao, L. Zhou, H. Zeng, S. Li, and X. Liu, "50-Gb/s/λ TDM-PON based on 10 G DML and 10 G APD supporting PR10 link loss budget after 20-km downstream transmission in the O-band," *2017 Optical Fiber Communications Conference and Exhibition (OFC)*, Los Angeles, CA, USA, 2017, pp. 1–3.
2. R. Borkowski, H. Schmuck, G. Cerulo, H. Debrégeas, and R. Bonk, "Single-Wavelength Symmetric 50 Gbit/s Equalization-Free NRZ IM/DD PON with up to 33 dB Loss Budget and Fiber Transmission over >40 km," *2019 Optical Fiber Communications Conference and Exhibition (OFC)*, 2019, pp. 1–3.
3. N. Suzuki, H. Miura, K. Matsuda, R. Matsumoto, and K. Motoshima, "100 Gb/s to 1 Tb/s Based Coherent Passive Optical Network Technology," J. Lightwave Technol. **36**(8), 1485–1491 (2018).
4. 4. J. Cheng, C. Xie, Y. Chen, X. Chen, M. Tang, and S. Fu, "Comparison of Coherent and IMDD Transceivers for Intra Datacenter Optical Interconnects," *Optical Fiber Communications Conference and Exhibition (OFC'2019)*, San Diego, CA, USA, Mar. 2019, W1F.2.
5. P.-S. Naseem, Z. Wang, S. H. Ahmad, S. Parvez, H.-S. Yang, H-S Chen, J. J.-S. Chang, J.-W. Huang, and Shi, "Top-illuminated Avalanche Photodiodes with Cascaded Multiplication Layers for High-Speed and Wide Dynamic Range Performance," J. Lightwave Technol. **40**(24), 7893–7900 (2022).
6. T. Beckerwerth, R. Behrends, F. Ganzer, P. Runge, and M. Schell, "Linearity Characteristics of Avalanche Photodiodes For InP Based PICs," IEEE J. Sel. Top. Quantum Electron. **28**(2: Optical Detectors), 1–8 (2022).
7. M. Nada, Y. Yamada, and H. Matsuzaki, "Responsivity-Bandwidth Limit of Avalanche Photodiodes: Toward Future Ethernet Systems," IEEE J. Sel. Top. Quantum Electron. **24**(2), 1–11 (2018).
8. M. Nada, F. Nakajima, T. Yoshimatsu, Y. Nakanishi, A. Kanda, T. Shindo, S. Tatsumi, H. Matsuzaki, and K. Sano, "Inverted p-down Design for High-Speed Photodetectors," Photonics **8**(2), 39 (2021).
9. Albis Optoelectronics AG, Moosstrasse 2a, 8803 Rueschlikon, Switzerland. (Product: APD20D1 on Submount).
10. T. Takeshita, Y. Hirota, T. Ishibashi, Y. Muramoto, T. Ito, Y. Tohmori, and H. Ito, "Degradation behavior of avalanche photodiodes with a mesa structure observed using a digital OBIC monitor," IEEE Trans. Electron Devices **53**(7), 1567–1574 (2006).
11. Nan-Wei Chen Naseem, Syed Hasan Parvez, Zohauddin Ahmad, Sean Yang, H.-S. Chen, Hsiang-Szu Chang, Jack Jia-Sheng Huang, and Jin-Wei Shi, "Enhancement of Bandwidth-Responsivity Product in High-Speed Avalanche Photodiodes with Optimized Flip-Chip Bonding Package for Coherent Detection," *2023 Optical Fiber Communications Conference and Exhibition (OFC)*, 2023, pp. 1–3.
12. Z. Ahmad, S.-I Kuo, Y.-C. Chang, R.-L. Chao, Y.-S. Naseem, Y.-J. Lee, H.-M. Hung, J. Chen, C. S. Chen, J.-W. Goh, and Shi, "Avalanche Photodiodes with Dual Multiplication Layers and Ultra-High Responsivity-Bandwidth Products for FMCW Lidar System Applications," IEEE J. Sel. Top. Quantum Electron. **28**(2: Optical Detectors), 1–9 (2022).
13. Z. Naseem, Y.-M. Ahmad, R.-L. Liao, P.-S. Chao, Y.-S. Wang, S. Lee, S.-Y. Yang, H.-S. Wang, H.-S. Chang, J. J.-S. Chen, E. Huang, Y.-H. Chou, J.-W. Jan, and Shi, "Avalanche Photodiodes with Dual Multiplication Layers for High-Speed and Wide Dynamic Range Performances," Photonics **8**(4), 98 (2021).
14. Z. Naseem, Y.-M. Ahmad, P.-S. Liao, S. Wang, S.-Y. Yang, H.-S. Wang, H.-S. Chang, J. J.-S. Chen, E. Huang, Y.-H. Chou, J.-W. Jan, and Shi, "Avalanche Photodiodes with Composite Charge-Layers for Low Dark Current, High-Speed, and High-Power Performance," IEEE J. Sel. Top. Quantum Electron. **28**(2: Optical Detectors), 1–10 (2022).
15. N. Li, R. Sidhu, X. Li, F. Ma, S. Demiguel, X. Zhen, A. L. Holmes Jr., J. C. Campbell, D. A. Tulchinsky, and K. J. Williams, "High-saturation-current InGaAs/InAlAs charge-compensated uni-traveling-carrier photodiode," phys. stat. sol. (a) **201**(13), 3037–3041 (2004).
16. J.-M. Wun, C.-H. Lai, N.-W. Chen, J. E. Bowers, and J.-W. Shi, "Flip-Chip Bonding Packaged THz Photodiode With Broadband High-Power Performance," IEEE Photonics Technol. Lett. **26**(24), 2462–2464 (2014).
17. K. C. Gupta, Ramesh Garg, Inder Bahl, and Prakash Bhartia, "*Microstrip Lines and Slotlines*", 2nd Edition, Artech House, Boston London, 1996.
18. B. Shi, F. Qi, P. Cai, X. Chen, Z. He, Y. Duan, G. Hou, T. Su, S. Li, W. Chen, C. Hong, R.-C. Yu, and D. Pan, "106 Gb/s Normal-Incidence Ge/Si Avalanche Photodiode with High Sensitivity," *2020 Optical Fiber Communications Conference and Exhibition (OFC)*, 2020, pp. 1–3.

Optics EXPRESS

19. E. Chao, B. Xiong, C. Sun, Z. Hao, J. Wang, L. Wang, Y. Han, H. Li, J. Yu, and Y. Luo, "D-Band MUTC Photodiodes With Flat Frequency Response," IEEE J. Sel. Top. Quantum Electron. **28**(2: Optical Detectors), 1–8 (2022).
20. K. Li, X. Xie, Q. Zhou, A. Beling, and J. C. Campbell, "High Power 20-GHz Photodiodes With Resonant Microwave Circuits," IEEE Photonics Technol. Lett. **26**(13), 1303–1306 (2014).
21. Ansys, INC. "High Frequency Simulation software," https://www.ansys.com/products/electronics/ansys-hfss.
22. F.-M. Kuo, M.-Z. Chou, and J.-W. Shi, "Linear-Cascade Near-Ballistic Uni-Traveling-Carrier Photodiodes with an Extremely High Saturation-Current-Bandwidth Product," J. Lightwave Technol. **29**(4), 432–438 (2011).
23. N.-W. Chen, H.-J. Tsai, F.-M. Kuo, and J.-W. Shi, "High-Speed W-Band Integrated Photonic Transmitter for Radio-Over-Fiber Applications," IEEE Trans. Microwave Theory Tech. **59**(4), 978–986 (2011).
24. M. Nada, Y. Yamada, and H. Matsuzaki, "A High-Linearity Avalanche Photodiodes with a Dual-Carrier Injection Structure," IEEE Photonics Technol. Lett. **29**(21), 1828–1831 (2017).
25. P. Runge, G. Zhou, T. Beckerwerth, F. Ganzer, S. Keyvaninia, S. Seifert, W. Ebert, S. Mutschall, A. Seeger, and M. Schell, "Waveguide Integrated Balanced Photodetectors for Coherent Receivers," IEEE J. Sel. Top. Quantum Electron. **24**(2), 1–7 (2018).
26. T. Okimoto, K. Ashizawa, H. Mori, K. Ebihara, K. Yamazaki, S. Okamoto, K. Horino, Y. Ohkura, H. Yagi, M. Ekawa, and Y. Yoneda, "106-Gb/s Waveguide AlInAs/GaInAs Avalanche Photodiode with Butt-joint Coupling Structure," *2022 Optical Fiber Communications Conference and Exhibition (OFC)*, 2022, pp. 01–03.
27. M. Huang, K. Lee, K. Magruder, O. Dosunmu, R. Haislmaier, H. Liao, W. Qian, P. Martin, J. Hicks, P. Patel, C. Brandt, and A. Liu, "200Gb/s per lane Ge/Si waveguide avalanche photodiode," in *European Conference on Optical Communication (ECOC) 2022*, J. Leuthold, C. Harder, B. Offrein, and H. Limberger, eds., Technical Digest Series (Optica Publishing Group, 2022), paper Th2E.2.
28. T. Beckerwerth, H. Boerma, T. T. Tran, F. Ganzer, P. Runge, and M. Schell, "High-Speed Waveguide Integrated Avalanche Photodiode for InP-PICs," *2022 IEEE Photonics Conference (IPC)*, Vancouver, BC, Canada, 2022, pp. 1–2.